Understanding Plasmon Coupling in Nanoparticle Dimers using Molecular Orbitals and Configuration Interaction

Fahri Alkan[a,b] and Christine M. Aikens[b,*]

a) Department of Material Science & Nanotechnology Engineering, Abdullah Gül University, Kayseri 38080, Turkey
b) Department of Chemistry, Kansas State University, Manhattan, KS 66506, USA
* cmaikens@ksu.edu; 1-785-532-0954

Abstract

We perform a theoretical investigation of the electronic structure and optical properties of atomic nanowire and nanorod dimers using DFT and TDDFT. In both systems at separation distances larger than 0.75 nm, optical spectra show a single feature that resembles the bonding dipole plasmon (BDP) mode. A configuration interaction (CI) analysis shows that the BDP mode arises from constructive coupling of transitions, whereas the destructive coupling does not produce significant oscillator strength for such separation distances. At shorter separation distances, both constructive and destructive coupling produce oscillator strength due to wave-function overlap, which results in multiple features in the calculated spectra. Our analysis shows that a charge-transfer plasmon (CTP) mode arises from destructive coupling of transitions, whereas the BDP results from constructive coupling of the same transitions at shorter separation distances. Furthermore, the coupling elements between these transitions are shown to depend heavily on the amount of exact Hartree-Fock exchange (HFX) in the functional, which affects the splitting of CTP and BDP modes. With 50% HFX or more, the CTP and BDP modes mainly merge into a single feature in the spectra. These findings suggest that the effects of exact exchange must be assessed during the prediction of CTP modes in plasmonic systems.

Introduction

Noble metal nanoparticles show distinct opto-electronic properties which result from surface plasmon resonance (SPR).[1–5] The resonance condition for SPR is highly tunable with nanoparticle size, shape or the dielectric properties of the medium.[6–9] The tunability of SPR offers many potential applications for metal nanoparticles in areas such as catalysis, biosensing or light-harvesting materials.[10–17] For the theoretical treatment of SPR, a variety of methodologies are available ranging from classical methods based on solving Maxwell equations to fully atomistic quantum mechanical simulations.[18–20] For a wide range of applications, SPR is well described by employing classical methods.[21–24] However, a classical description of SPR can be problematic for cases such as nanoparticle assemblies with subnanometer gaps,[25–28] or when the particle radius is less than 5-10 nm.[29,30] For such systems, one needs to account for the quantum nature of electronic motion.

In the case of a nanoparticle dimer, the optical response of the system is altered compared to the case for a single nanoparticle as a result of plasmon coupling.[22,31–34] For long separation distances, plasmon coupling can be described by methods such as plasmon hybridization.[23,35,36] In this regime, an attractive interaction between two plasmons form a bonding dipole plasmon (BDP), which monotonically redshifts with decreasing gap distance.[22,23,32] However, the classical picture for plasmon interaction breaks down when the separation distance is below 1 nm.[25,26,34] In this range, quantum mechanical effects can introduce a redshift-to-blueshift crossover. Furthermore, a new plasmon mode called the charge transfer plasmon (CTP) resulting from quantum tunneling of electrons between two particles is predicted in the spectra.[37,38]
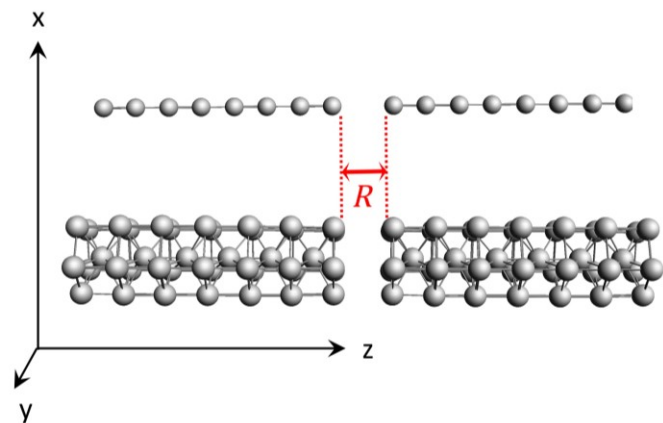
Several theoretical approaches have been proposed in the literature in order to predict plasmonic properties of nanoparticles in the quantum regime. Earlier efforts often employed jellium model,[39–41] where the potential from atomic nuclei are approximated by a uniform charge distribution. Despite its relative simplicity, jellium calculations have been crucial for the understanding of quantum effects in plasmonic systems such as spill-out effects or quantum tunneling effects.[27,42–46] More recently, atomistic methods with explicit basis functions have been employed to investigate such effects.[47–55] These investigations have mainly focused on the optical properties of single nanoparticles. In comparison, atomistic TDDFT investigations of plasmonic coupling have been rather limited,[56–59] and plasmon coupling for small nanoparticle gap distances is not well understood from a wave-function point of view. Furthermore, TDDFT investigations for the optical response of metallic nanoparticles have generally been carried out using LDA and GGA type density functionals, primarily due to their low computational cost and good accuracy for describing monomeric metallic systems. However, local or semi-local density functionals such as LDAs and GGAs are known to be problematic for a number of cases, particularly for excited states involving charge transfer.[60–64] Therefore, the accuracy of local DFT functionals should also be examined for the description of plasmon coupling in a nanoparticle dimer, especially for CTP.

In this work, we will address these issues for the plasmonic coupling in nanoparticle dimers using molecular orbital (MO) theory and a configuration interaction (CI) method. Silver atomic chain (Ag_8) and nanorod (Ag_{41}^{-1}) dimers are investigated as model systems. These nanoparticles are much smaller than the typical nanorods investigated in experimental work; however, theoretical investigations with similar systems have provided important insights into quantum plasmonics.[47,58,65] In the first part our investigation, we investigate the origin of CTP and BDP modes from a molecular orbital and configuration interaction view. The second part of the investigation examines whether the distinction between these modes are still present with different DFT approaches, specifically hybrid functionals with varying exchange. Our results will hopefully

provide a CI framework for CTP and BDP modes in plasmonic systems, as well as raise some important questions for the prediction of these modes using various DFT approaches.

Computational Methods

All calculations were performed using the ADF2017 package.[66–68] Dimer assemblies of the neutral Ag_8 nanowire and Ag_{41}^{-1} nanorod anion were chosen as model systems as illustrated in Figure 1. The geometries of the monomers were optimized using the BP86[69,70] functional and double zeta (DZ) (large frozen core) basis set, whereas dimers were set up from the optimized geometries of the monomers with a given gap distance. We note that the geometries obtained with PBE[71] and B3LYP[72,73] functionals for the Ag_8 system are quite similar to the results obtained with the BP86 functional, and the resulting optical spectra from these geometries for the test cases are almost identical as shown in Figure S1. To be consistent with the geometries from previous studies,[48,74] BP86 has remained the functional of choice for the rest of the systems investigated. The performance of the DZ basis set for the description of plasmon coupling is also tested by comparing the results for Ag_8 nanowires at various gap distance obtained with the triple-zeta polarization (TZP) basis set as shown in Figure S2. Employing a larger basis set has very little effect on the calculated spectra in these cases. The point group symmetries of the Ag_8 and Ag_{41}^{-1} dimers are $D_{\infty h}$ and D_{5h} respectively for the investigated systems. In our investigation, only end-to-end dimers of nanorods and nanowires are considered since the CTP mode is not observed for the longitudinal peak (polarization along the long axis of nanorods and nanowires) of side-by-side assemblies in our previous work.[59] The molecular orbitals of monomeric nanowires and nanorods are labelled as $nm_{g/u}$ using cylindrical symmetry, where n denotes the axial quantum number, m denotes σ or π and g/u shows the inversion symmetry of the orbital. For the dimeric orbitals, we use the capital Greek letters Σ or Π. The optical spectra were calculated with PBE[71], BLYP[69,73] and B3LYP[72,73] functionals as mentioned in the text. The excited states were calculated using the TDDFT formalism except for the BLYP and B3LYP calculations of Ag_{41}^{-1} dimers. For these calculations, we employed the simplified-TDDFT[75,76] formalism as implemented in ADF. The number of calculated excited states for all systems are chosen so that the energies of these states cover the 0.0-4.0 eV range for the optical spectra. The optical spectra were obtained by employing a 0.2 eV full-width-half-maximum (FWHM) Gaussian broadening. To calculate one-electron configuration excited states, we employed a restricted TDDFT approach available in ADF, where only a selected occupied-virtual pair was used for the TDDFT calculation.
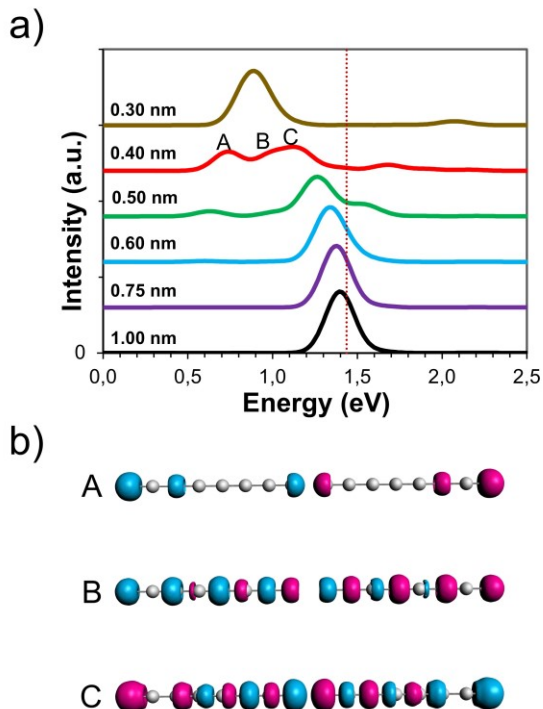
Figure 1. End-to-end assemblies of the Ag_8 (top) and Ag_{41}^{-1} (bottom) dimers investigated in this work. The gap distance is defined as the nearest Ag-Ag distance in the assemblies as shown in the figure.

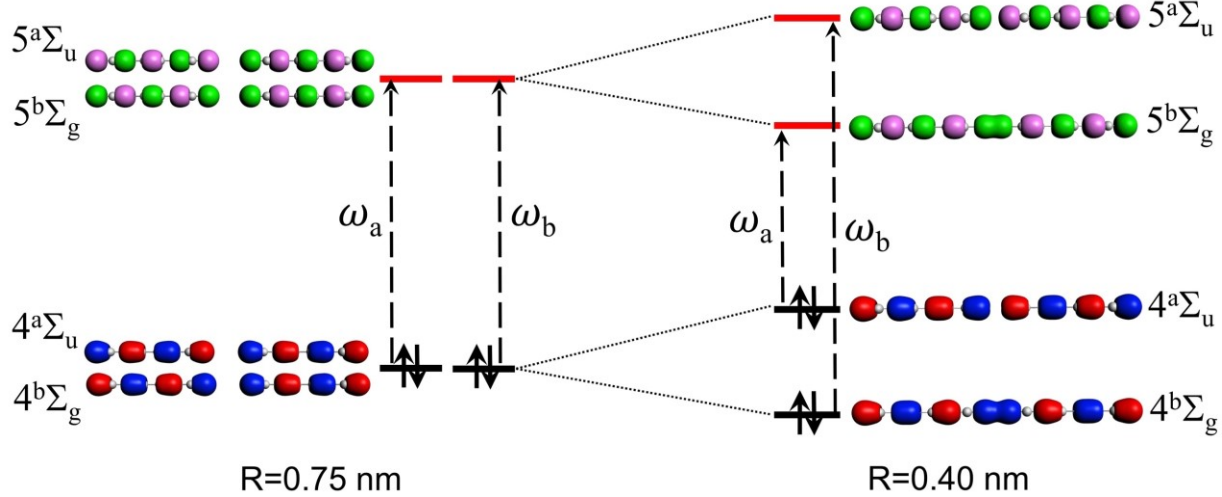## Results and Discussion

Atomic nanowire

In Figure 2a, we show the calculated spectra at the PBE/DZ level of theory for the Ag_8 nanowire dimers with gap distances between 1.00-0.30 nm. In this energy range (0.0-2.5 eV), the spectra only show polarization along the long (z) axis of the wires. For the interparticle distance of 1.00 nm, calculated spectra show an intense feature around 1.4 eV. This peak is slightly redshifted compared to the case in monomer due to the attractive coupling between plasmon modes on individual rods as predicted by the classical plasmon hybridization model.[23,77] As the gap distance becomes smaller, this redshift generally increases; however, new features also arise in the spectra when the gap distance is smaller than 0.60 nm. The splitting for the peaks becomes particularly noticeable when the gap distance is 0.40 nm. Figure 2b illustrates the calculated transition-fit densities (TFD) of the excited states at this gap distance. It is seen that the low-energy feature around 0.7 eV (peak A) shows a strong charge transfer plasmon (CTP) character, whereas the higher-energy feature around 1.2 eV (peak C) can be described as a bonding dipole plasmon (BDP) mode. In comparison, the feature between these modes (~1.0 eV, peak B) mainly shows a mixture of both CTP and BDP character. At the 0.30 nm gap distance, the spectra again exhibit a single feature around 0.8 eV, similar to the single peak observed at long separation distances. It should be noted that this gap distance is comparable to the Ag-Ag bond distances (~0.28 nm) for the monomer, and as a result the optical response of the Ag_8 dimer behaves similar to a monomeric Ag_{16} nanorod at this gap distance.

Figure 2. a) Calculated spectra with PBE/DZ level of theory for Ag_8 atomic wire dimers at gap distances between 1.00 and 0.30 nm (the red dotted line corresponds to the monomer plasmonic peak at 1.4 eV) and b) calculated transition-fit densities (TFD) of excited states for the dimer with gap distance of 0.40 nm. TFDs from top to bottom corresponds

to the excited states at 0.74 (A), 0.99 (B) and 1.15 eV (C), respectively. All calculations were performed with the PBE/DZ(frozen core) level of theory.

In previous work with monomer systems, it has been shown that the longitudinal peak of nanowires mainly arises from $n\sigma_{g/u}\rightarrow(n+1)\sigma_{u/g}$ type transitions.[53,74] In the case of the Ag_8 nanorod, this transition corresponds to $4\sigma_u\rightarrow5\sigma_g$. For the dimers, longitudinal peaks arise from transitions between dimeric orbitals, which are linear combinations of monomeric $4\sigma_u$ and $5\sigma_g$ levels as shown in Figure 3. Due to the inversion symmetry around the gap center, the allowed transitions are $|4\sigma_u+4\sigma_u|$ (bonding) $\rightarrow$ $|5\sigma_g-5\sigma_g|$ (antibonding), and $|4\sigma_u-4\sigma_u|$ (antibonding) $\rightarrow$ $|5\sigma_g+5\sigma_g|$ (bonding), which are abbreviated $4^b\Sigma_g\rightarrow5^a\Sigma_u$ and $4^a\Sigma_u\rightarrow5^b\Sigma_g$. In this notation, capital sigma denotes the dimeric orbital, and superscripts "b" or "a" correspond to the bonding or antibonding combinations of the monomeric orbitals, respectively. The other two possible configurations ($4^a\Sigma_u\rightarrow5^a\Sigma_u$ and $4^b\Sigma_g\rightarrow5^b\Sigma_g$) are symmetry forbidden. The electronic structure of Ag_8 dimers show that occupied $4^a\Sigma_u$ and $4^b\Sigma_g$ levels exhibit near-degeneracy at 1.00 and 0.75 nm gap distances (Figure 3, left). This is also the case for unoccupied $5^b\Sigma_g$ and $5^a\Sigma_u$ levels. However, this near-degeneracy becomes lifted at shorter gaps as the overlap between monomeric orbitals becomes significant, and bonding and antibonding interactions become energetically different (Figure 3, right).

Figure 3. Schematics of the interaction picture between occupied and unoccupied levels of Ag_8 atomic wire dimers with changing gap distance. At 0.75 nm, there is little overlap between monomeric orbitals, which results in nearly degenerate $4^a\Sigma_u$ and $4^b\Sigma_g$ levels for HOMO and $5^b\Sigma_g$ and $5^a\Sigma_u$ levels for LUMO. This near-degeneracy is broken as a result of significant overlap for shorter distances as shown for 0.40 nm. The dipole-allowed transitions ($4^a\Sigma_u\rightarrow5^b\Sigma_g$ and $4^b\Sigma_g\rightarrow5^a\Sigma_u$) are shown with dashed lines.

Table 1 shows selected excited states where $4^a\Sigma_u\rightarrow5^b\Sigma_g$ and $4^b\Sigma_g\rightarrow5^a\Sigma_u$ configurations contribute significantly for the gap distances 0.75 nm and 0.40 nm. At the 0.75 nm gap distance, $4^a\Sigma_u\rightarrow5^b\Sigma_g$ and $4^b\Sigma_g\rightarrow5^a\Sigma_u$ transitions mix evenly due to configuration interaction, which results in two excited states. The low energy excited state corresponds to the destructive interaction because the dipole moments from each configuration essentially cancel out. In comparison, the dipole moments of these configurations are additive for the high energy excited state. The interaction picture of these two configurations can be understood qualitatively by configuration interaction Hamiltonian in a 2x2 matrix form[78]:

$$\begin{bmatrix} \alpha_{11} & \beta_{12} \\ \beta_{21} & \alpha_{22} \end{bmatrix} \tag{1}$$

where α_{ii} are on-site elements for one configuration, and β_{ij} corresponds to the coupling between two different configurations. For the 0.75 nm gap, we can assume that $\alpha_{11}=\alpha_{22}=\alpha$, since both configurations are approximately degenerate as shown in Figure 3. Moreover, we can also set $\beta_{12}=\beta_{21}=\beta$ for the off-diagonal elements when the orbitals are real. These approximations lead to the following solutions for the excited states Ψ_1 and Ψ_2:

$$\Psi_1 = \frac{1}{\sqrt{2}}(\phi_a - \phi_b) \text{ with } E_1 = \alpha - \beta \tag{2}$$

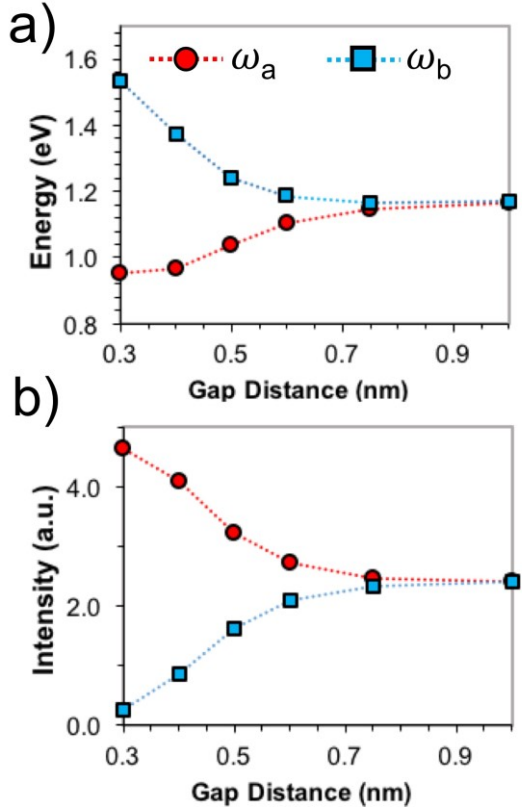$$\Psi_2 = \frac{1}{\sqrt{2}}(\phi_a + \phi_b) \text{ with } E_2 = \alpha + \beta \tag{3}$$

Here, ϕ_a and ϕ_b denote the configurations (Slater determinants) corresponding to $4^a\Sigma_u \rightarrow 5^b\Sigma_g$ and $4^b\Sigma_g \rightarrow 5^a\Sigma_u$ transitions respectively. For this case, the $\Psi_0 \rightarrow \Psi_1$ excitation does not produce intensity since the dipole moment contribution from each contribution is cancelled out perfectly. In comparison, the $\Psi_0 \rightarrow \Psi_2$ excitation should give a large intensity since the dipole-moment contributions are additive for this case. As shown in Table 1, the results obtained from TDDFT calculations for the 0.75 nm gap show a good agreement with this interaction picture. Here, the excited state with 0.60 eV energy from the TDDFT calculations corresponds approximately to $\Psi_0 \rightarrow \Psi_1$ with energy E_1 (α–β) in Eq. 2 as this state results from destructive coupling of $4^a\Sigma_u \rightarrow 5^b\Sigma_g$ and $4^b\Sigma_g \rightarrow 5^a\Sigma_u$ transitions. Similarly, the excited state with an energy of 1.37 eV corresponds to $\Psi_0 \rightarrow \Psi_2$ with energy E_2 (α+β) in Eq. 3 as this state results from the constructive coupling of the same configurations. Additionally, the TDDFT results suggest a positive β between these configurations since the destructive mixing (Ψ_1) corresponds to the lower-energy state. We will see in the following discussions that this is not always the case when we introduce hybrid functionals with exact exchange.

Table 1. Calculated Energies, Intensities, and Important Configurations with Weights and Dipole Moment Contributions with PBE/DZ Level of Theory for Selected Excited States of Ag_8 Dimers at 0.75 nm Gap Distance and 0.40 nm Gap Distance.

Excited State	Energy (eV)	Oscillator Strength (a.u.)	Transitions	Weight	Contribution to Transition Dipole Moment (a.u.)
0.75 nm Gap Distance					
1	0.60	0.00	$4^a\Sigma_u \rightarrow 5^b\Sigma_g$	0.51	9.31
			$4^b\Sigma_g \rightarrow 5^a\Sigma_u$	0.49	-8.84
2	1.37	4.21	$4^b\Sigma_g \rightarrow 5^a\Sigma_u$	0.47	5.70
			$4^a\Sigma_u \rightarrow 5^b\Sigma_g$	0.45	5.75
0.40 nm Gap Distance					
1	0.74	1.33	$4^a\Sigma_u \rightarrow 5^b\Sigma_g$	0.66	-12.22
			$4^b\Sigma_g \rightarrow 5^a\Sigma_u$	0.29	3.70
2	0.99	1.10	$4^a\Sigma_u \rightarrow 5^b\Sigma_g$	0.16	-5.26
			$4^b\Sigma_g \rightarrow 5^a\Sigma_u$	0.11	-1.96
3	1.15	1.43	$4^b\Sigma_g \rightarrow 5^a\Sigma_u$	0.33	3.13
			$4^a\Sigma_u \rightarrow 5^b\Sigma_g$	0.13	4.38

As the gap distance become smaller, we deviate significantly from the configuration interaction solutions shown in eq. 2 and 3, since both energies and transition dipole moment contributions of each configuration become different as a result of non-zero overlap between monomeric orbitals. This is illustrated in Figure 4 where we compare the TDDFT predictions for the excited state energies and intensities for each one-electron configuration using selected occupied-virtual pairs. At longer gap distances such as 0.75 nm or 1.00 nm, both calculated energies and intensities from each configuration are quite similar as expected from the electronic structure shown in Figure 4. With decreasing gap distance, the predicted energy becomes smaller whereas the intensity becomes larger for the $4^a\Sigma_u \rightarrow 5^b\Sigma_g$ state. In comparison, the situation is opposite for the $4^b\Sigma_g \rightarrow 5^a\Sigma_u$ state. At 0.40 nm, the calculated intensity ratio for these states is around 5 and the calculated energy difference is 0.41 eV. For the 0.30 nm gap distance, the intensity ratio becomes ~18. This suggests that the $4^a\Sigma_u \rightarrow 5^b\Sigma_g$ configuration is significantly more dominant for the strong spectral feature shown in Figure 2 at this gap distance.

When the near-degeneracy is lifted for the energies and intensities of the $4^a\Sigma_u \rightarrow 5^b\Sigma_g$ and $4^b\Sigma_g \rightarrow 5^a\Sigma_u$ configurations such as that observed with the 0.40 nm gap, the calculated spectra show drastic differences when compared to the case of the 0.75 nm or 1.00 nm gap distance. For the 0.40 nm gap, the destructive coupling between the configurations produces a large-intensity excited state at 0.74 eV (Table 1), since the transition dipole moment contributions of these configurations are quite different. In fact, this destructive coupling produces the strong CTP mode for this system as shown in Figure 2b. In comparison, the excited states at 0.99 eV and 1.15 eV both result from a constructive mixing of each configuration (Table 1). We note that other configurations also contribute to these excited states; however, the resulting transition dipole moments are largely from the $4^a\Sigma_u \rightarrow 5^b\Sigma_g$ and $4^b\Sigma_g \rightarrow 5^a\Sigma_u$ configuration.
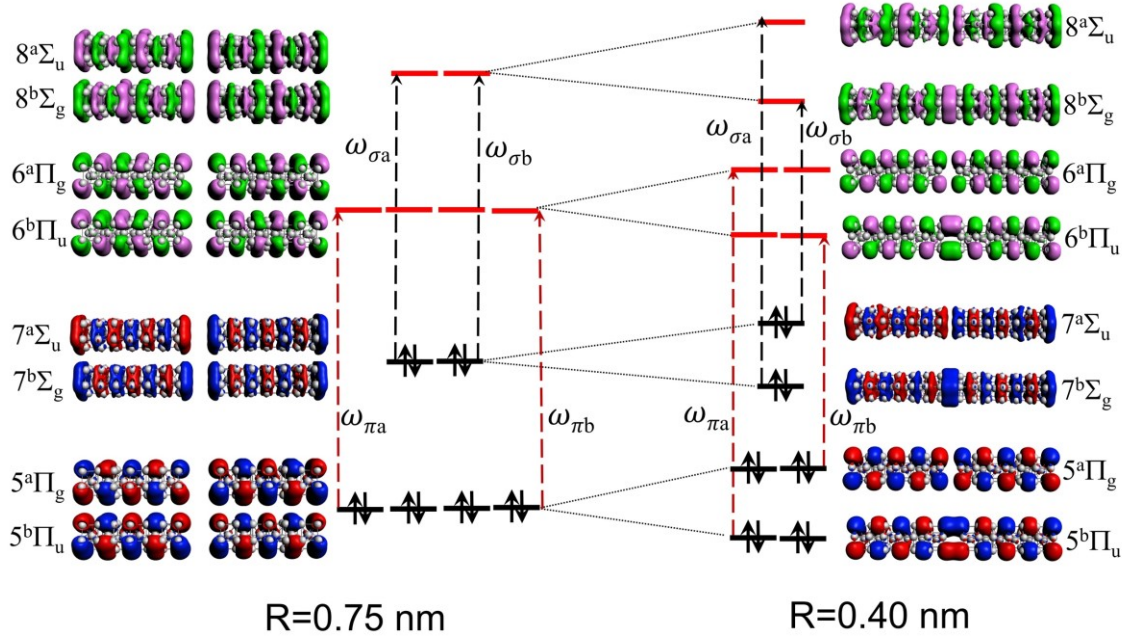
Figure 4. Comparison of a) energies and b) intensities for the one-electron transitions of $4^a\Sigma_u \rightarrow 5^b\Sigma_g$ (ω_a) and $4^b\Sigma_g \rightarrow 5^a\Sigma_u$ (ω_b) calculated with restricted TDDFT at the PBE/DZ level of theory.

In addition to the 0.40 nm gap distance, we have analyzed the calculated TFDs for 1.00, 0.75 and 0.50 nm gap distances as shown in Figure S3 and Table S1 of the supporting information (SI). In all cases, constructive coupling of the configurations produces a large-intensity excited state that is similar to the BDP mode predicted in classical plasmon hybridization model, whereas the destructive coupling of the same configurations results in the CTP mode, which typically has a lower oscillator strength. In the case of 0.75 nm and 1.00 nm gap distances, the CTP mode has nearly zero intensity (Table 1) due to cancellation of oscillator strength in the destructive mixing. However, the CTP mode gains intensity with decreasing gap distance as a result of wave-function overlap between the monomeric orbitals and the resulting configuration interaction. These results provide the origin for the CTP and BDP modes in the case of nanowires from the configuration-interaction perspective.
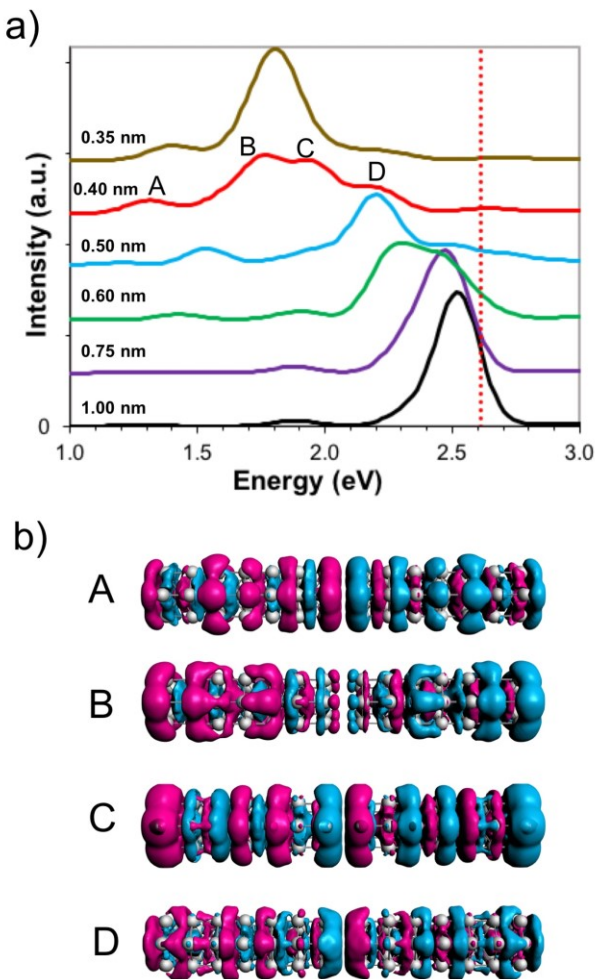
Cylindrical nanorod

Now, we turn our attention to Ag_{41}^{-1} dimers (Figure 1) to understand the size evolution of plasmon coupling. For the monomer, TDDFT predicts a large-intensity longitudinal peak at 2.61 eV. Similar to the case in nanowires, a $7\sigma_g \rightarrow 8\sigma_u$ type transition contributes significantly to the dipole moment of the excited state responsible for the longitudinal peak. Although this sigma transition is the only important one for small nanowires, a $5\pi_u \rightarrow 6\pi_g$ type transition also exhibits a large contribution to the dipole moment of the longitudinal peak in this larger nanorod.[48,53] In Figure 5, we illustrate the interaction picture for dimer orbitals and the resulting electronic structure for the Ag_{41}^{-1} dimers at 0.75 nm and 0.40 nm gap distances. At 0.75 nm or longer gap distances, $7^b\Sigma_g$ and $7^a\Sigma_u$ levels mainly exhibit a two-fold degeneracy, whereas $5^b\Pi_u$ and $5^a\Pi_g$ show an approximate four-fold degeneracy. This is also the case for the corresponding unoccupied levels as shown in Figure 5. As the separation distance become smaller, these near-degeneracies becomes lifted significantly, similar to the case in Ag_8 nanowire dimers. At the 0.40 nm gap distance, the energy differences between bonding and antibonding combinations of occupied Σ and Π levels are 0.4 eV and 0.2 eV, respectively, which suggests that the orbital coupling is more efficient for the Σ levels as expected. This is also seen for the unoccupied levels. Due to the symmetry of the dimer, dipole-allowed configurations correspond to $7^a\Sigma_u \rightarrow 8^b\Sigma_g$, $7^b\Sigma_g \rightarrow 8^a\Sigma_u$, $5^a\Pi_g \rightarrow 6^b\Pi_u$ and $5^b\Pi_u \rightarrow 6^a\Pi_g$ as illustrated in Figure 5. Since the allowed configurations correspond to bonding→antibonding or antibonding→bonding, the one-electron energies and intensities of these transitions are altered when the gap distances become shorter, similar to the case in nanowires.

Figure 5. Schematics of the interaction picture between occupied and unoccupied levels of Ag_{41}^{-1} nanorod dimers with changing gap distance. Dotted red and black lines show the dipole allowed $\Pi \rightarrow \Pi$ and $\Sigma \rightarrow \Sigma$ configurations respectively.

In Figure 6a, we show the calculated absorption spectra of Ag_{41}^{-1} dimers for varying gap distances. For 1.00 nm and 0.75 nm gaps, the dimer spectra mainly show an intense peak that is redshifted compared to the peak for the monomer. This is again expected from the classical predictions based on the plasmon hybridization model. The redshift in cylindrical nanorods is slightly larger compared to the case in nanowires (Figure 1), which is most likely due to the larger size of the former. As the gap distance become smaller than 0.75 nm, new features arise in the spectra as a result of wave-function overlap. These features start to merge into a single peak at the 0.35 nm gap distance as the combined system now resembles a single nanorod. Overall, the results for the cylindrical nanorods are quite similar to the results obtained for the nanowires.

a)

b)

Figure 6. a) Calculated spectra with PBE/DZ level of theory for Ag_{41}^{-1} nanorod dimers at gap distances between 1.00 and 0.35 nm and b) calculated TFDs for the selected excited states for the dimer with gap distance of 0.40 nm. TFDs correspond to the excited states at 1.32, 1.76, 1.96 and 2.21 eV from top to bottom respectively.

For the 0.40 nm gap distance, the splitting of the longitudinal peak is the most noticeable similar to the case in nanowires. At this separation distance, the absorption spectrum mainly exhibits four features in the displayed energy range. The calculated TFDs for these features are illustrated in Figure 6b. It is seen that the excited states around 1.32 and 1.76 eV have more CTP character because the opposite charge densities are more localized on the individual monomers. In comparison, the calculated TFDs exhibit more BDP character for the excited states around 1.96 and 2.21 eV because the tip part of each monomer has opposite charges along the z axis, which creates a dipole for each individual monomer in addition to the overall dipole for the dimer.

Table 2 shows the selected excited state configurations for the Ag_{41}^{-1} dimer systems at 0.75 nm and 0.40 nm gap distances from full TDDFT calculations. At the 0.75 nm gap, TDDFT predicts three excited states with energies 1.03, 1.28 and 1.37 eV where the contribution from the aforementioned Σ and Π levels are quite significant. However, the calculated oscillator strength for these states are negligible due to the cancellation of transition dipole moments via destructive mixing. For the excited state at 2.50 eV, the configurations mix constructively, which results in a high oscillator strength as shown in Table 2. The energy of the state arising from a fully

constructive mixing of configurations is considerably higher compared to the destructive coupling states. This suggests that coupling matrix elements between configurations are again positive as in the case of nanowires. At 0.40 nm separation, both constructive and destructive mixing of configurations result in excited states with significant oscillator strength. For the excited states at 1.32 and 1.76 eV respectively, $5^b\Pi_u \rightarrow 6^a\Pi_g$ and $7^b\Sigma_g \rightarrow 8^a\Sigma_u$ configurations contribute destructively to the transition dipole moments of the excited states. We also note that the calculated TFDs for these states exhibit a strong CTP character. In comparison, the configurations mix constructively for the excited states at 1.96 and 2.21 eV, which have more BDP character. This is also similar to the case in nanowires, where the destructive and constructive mixing of configurations are responsible for CTP and BDP respectively.

Table 2. Calculated Energies, Intensities, and Important Configurations with Weights and Dipole Moment Contributions for the Selected Excited States of Ag_{41}^{-1} Dimers at 0.75 nm Gap Distance and 0.40 nm Gap Distance.

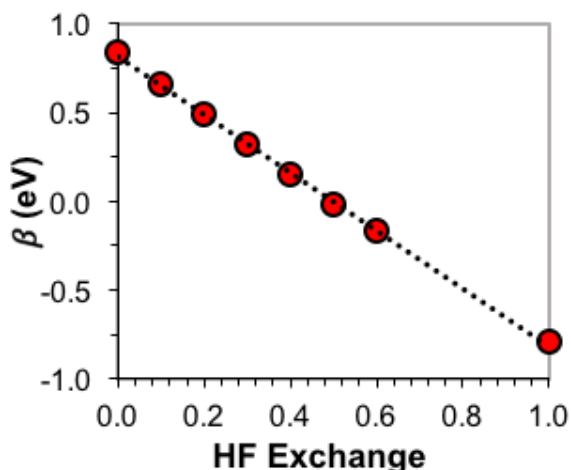| Excited State #	Energy (eV)	Oscillator Strength (a.u.)	Transitions	Weight	Contribution to Transition Dipole Moment
			0.75 nm Gap Distance		
1	1.03	0.01	$5^a\Pi_g \rightarrow 6^b\Pi_u$	0.51	11.77
			$5^b\Pi_u \rightarrow 6^a\Pi_g$	0.48	-10.97
2	1.28	0.07	$7^a\Sigma_u \rightarrow 8^b\Sigma_g$	0.48	-8.68
			$5^b\Pi_u \rightarrow 6^a\Pi_g$	0.18	6.07
			$5^a\Pi_g \rightarrow 6^b\Pi_u$	0.15	5.70
			$7^b\Sigma_g \rightarrow 8^a\Sigma_u$	0.11	-3.84
3	1.37	0.08	$7^b\Sigma_g \rightarrow 8^a\Sigma_u$	0.59	-8.56
			$7^a\Sigma_u \rightarrow 8^b\Sigma_g$	0.22	5.62
			$5^b\Pi_u \rightarrow 6^a\Pi_g$	0.02	2.07
			$5^a\Pi_g \rightarrow 6^b\Pi_u$	0.02	2.05
4	2.50	10.91	$5^b\Pi_u \rightarrow 6^a\Pi_g$	0.10	-3.15
			$5^a\Pi_g \rightarrow 6^b\Pi_u$	0.09	-3.19
			$7^b\Sigma_g \rightarrow 8^a\Sigma_u$	0.08	-2.40
			$7^a\Sigma_u \rightarrow 8^b\Sigma_g$	0.07	-2.40
			0.40 nm Gap Distance		
1	1.32	1.68	$5^b\Pi_u \rightarrow 6^a\Pi_g$	0.44	6.08
			$7^a\Sigma_u \rightarrow 8^b\Sigma_g$	0.16	-5.88
			$5^a\Pi_g \rightarrow 6^b\Pi_u$	0.10	-5.73
2	1.76	6.75	$7^b\Sigma_g \rightarrow 8^a\Sigma_u$	0.31	2.74
			$7^a\Sigma_u \rightarrow 8^b\Sigma_g$	0.09	-3.94
			$5^a\Pi_g \rightarrow 6^b\Pi_u$	0.13	-5.61
			$5^b\Pi_u \rightarrow 6^a\Pi_g$	0.07	-2.14
3	1.96	4.24	$7^b\Sigma_g \rightarrow 8^a\Sigma_u$	0.23	-2.24
			$7^a\Sigma_u \rightarrow 8^b\Sigma_g$	0.03	-2.23
			$5^a\Pi_g \rightarrow 6^b\Pi_u$	0.04	-3.01
			$5^b\Pi_u \rightarrow 6^a\Pi_g$	0.02	-1.13
4	2.21	2.84	$5^a\Pi_g \rightarrow 6^b\Pi_u$	0.02	-2.01
			$7^b\Sigma_g \rightarrow 8^a\Sigma_u$	0.02	-0.54
			$7^a\Sigma_u \rightarrow 8^b\Sigma_g$	0.01	-1.30
			$5^b\Pi_u \rightarrow 6^a\Pi_g$	0.01	-0.81

Hybrid functionals

To understand how these findings can vary with different DFT approaches, we have performed TDDFT calculations on our model systems using the B3LYP functional with varying exact Hartree-Fock exchange (HFX) between 10% and 60%. For the comparison with 0% HFX, we have employed the BLYP functional. For the Ag_8 nanowire dimer, it is seen that $4^a\Sigma_u \rightarrow 5^b\Sigma_g$ and $4^b\Sigma_g \rightarrow 5^a\Sigma_u$ configurations are mainly responsible for the longitudinal plasmon-like polarization with the B3LYP functional as well. In Table 3, we show the destructive and constructive couplings of these configurations at a 0.75 nm gap distance for BLYP, B3LYP-20%, B3LYP-40% and B3LYP-60% from TDDFT calculations. At this gap distance, the simplified configuration interaction Hamiltonian and solutions given in Eq. 1-3 still provide a very good approximation for the TDDFT calculations. We note that the results obtained with BLYP show excellent agreement compared to the PBE results. With BLYP, the energy difference between the states arising from constructive and destructive coupling is 0.79 eV, with the former being higher in energy. When B3LYP is employed with 20% HFX, this energy difference decreases to 0.37 eV. For B3LYP-40% and B3LYP-60%, the ordering of constructive and destructive coupling is reversed compared to the case in BLYP and B3LYP-20%, resulting in energy differences of 0.11 and 0.68 eV respectively.

Table 3. The Effect of HFX Percentage in the Functional on the Calculated Excited States for Ag_8 Dimers at 0.75 nm Gap Distance

Excited State #	Energy (eV)	Oscillator Strength (a.u.)	Transitions	Weight	Contribution to Transition Dipole Moment
			BLYP		
1	0.59	0.00	$4^a\Sigma_u \rightarrow 5^b\Sigma_g$	0.51	9.31
			$4^b\Sigma_g \rightarrow 5^a\Sigma_u$	0.49	-8.84
2	1.38	4.21	$4^b\Sigma_g \rightarrow 5^a\Sigma_u$	0.47	-5.76
			$4^a\Sigma_u \rightarrow 5^b\Sigma_g$	0.45	-5.80
			B3LYP-20%		
1	0.98	0.01	$4^a\Sigma_u \rightarrow 5^b\Sigma_g$	0.52	-8.58
			$4^b\Sigma_g \rightarrow 5^a\Sigma_u$	0.47	8.10
2	1.35	4.47	$4^b\Sigma_g \rightarrow 5^a\Sigma_u$	0.52	-5.99
			$4^a\Sigma_u \rightarrow 5^b\Sigma_g$	0.47	-5.71
			B3LYP-40%		
1	1.35	4.63	$4^a\Sigma_u \rightarrow 5^b\Sigma_g$	0.57	-6.48
			$4^b\Sigma_g \rightarrow 5^a\Sigma_u$	0.40	-5.06
2	1.46	0.03	$4^b\Sigma_g \rightarrow 5^a\Sigma_u$	0.58	8.03
			$4^a\Sigma_u \rightarrow 5^b\Sigma_g$	0.40	-7.17
			B3LYP-60%		
1	1.34	4.77	$4^a\Sigma_u \rightarrow 5^b\Sigma_g$	0.48	-5.79
			$4^b\Sigma_g \rightarrow 5^a\Sigma_u$	0.45	-5.50
2	2.02	0.07	$4^b\Sigma_g \rightarrow 5^a\Sigma_u$	0.50	-6.99
			$4^a\Sigma_u \rightarrow 5^b\Sigma_g$	0.47	6.91

If one examines Eq. 1-3 carefully, it is clear that the energy gap between constructive and destructive coupling states are directly related to off-diagonal coupling elements (β) between the configurations. This coupling is predicted to be positive for GGA functionals where HFX=0%. As the amount of HFX increases in the functional, the value of this coupling becomes smaller, and finally shifts to negative values. As a result, the energy gap and ordering for constructive and
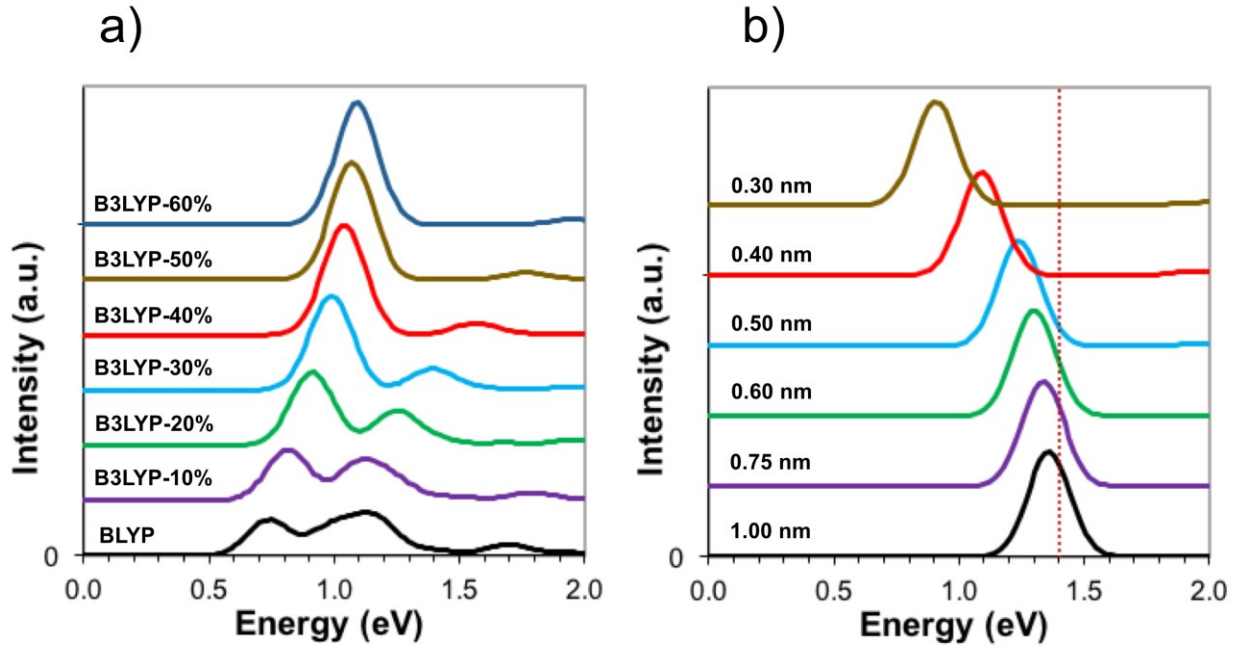
destructive coupling states are affected significantly by the amount of HFX in the functional This is illustrated in Figure 7, where the variation of calculated off-diagonal coupling element (β) with respect to HFX is given using the Tamm-Dancoff approximation (TDA) and a truncated occupied-unoccupied space that covers the $4^a\Sigma_u \rightarrow 5^b\Sigma_g$ and $4^b\Sigma_g \rightarrow 5^a\Sigma_u$ configurations. The set-up for these calculations is described in more detail in the SI. Surprisingly, this alteration in the coupling interaction has little effect on the calculated spectra for the 0.75 nm gap distance, since the energy and intensity of the excited state that results from constructive mixing vary only slightly for GGA functionals or hybrids as shown in Table 3.

Figure 7. The variation for the off-diagonal coupling element (β) with respect to the amount of HFX in the functional. For these calculations, 0.0 HFX corresponds to the BLYP functional whereas 1.0 HFX corresponds to the Hartree-Fock level of theory.

The results in Table 3 show that the energy and the intensity of the longitudinal peak exhibit a slight variation with respect to the amount of HFX in the level of theory at a gap distance of 0.75 nm. However, this is not the case when the gap distance is reduced to 0.40 nm as shown in Figure 8a. For this gap distance, the calculated spectra depend significantly on the choice of functional. With BLYP, the spectrum shows several features that are in excellent agreement with the previous results obtained with PBE. As the amount of HFX increases, the spectral features are generally predicted to lie higher in energy as the predicted HOMO-LUMO gap increases significantly with increasing HFX in the functional. More importantly, the set of several features predicted with GGA functionals merge into a single peak with increasing HFX. This result is most striking when the HFX percentage is 40% or more. To understand the effect of HFX in more detail, we also tabulate the energy, intensity and the configuration interaction for the excited states calculated with 0%, 20%, 40% and 60% HFX in Table 4. As it can be seen, the calculation with 0% HFX (BLYP) shows 3 states with high oscillator strength. As previously shown for the case with PBE, the excited state at 0.74 eV, which arises from the destructive mixing of $4^a\Sigma_u \rightarrow 5^b\Sigma_g$ and $4^b\Sigma_g \rightarrow 5^a\Sigma_u$ configurations, has a strong CTP character. In comparison, the excited states at 0.99 and 1.16 eV arise from constructive mixing of $4^a\Sigma_u \rightarrow 5^b\Sigma_g$ and $4^b\Sigma_g \rightarrow 5^a\Sigma_u$ configurations, and have more BDP character. When the amount of HFX is 20%, these states are predicted to be higher in energy by ~0.2 eV. While the energy ordering of the constructive and destructive mixing states remains the same compared to BLYP, the relative weights of the configurations are altered significantly in B3LYP-20%. At 40% HFX, the energy ordering of constructive and destructive mixing states changes compared to the cases with 0% or 20% HFX. At this point, the mixing of $4^a\Sigma_u \rightarrow 5^b\Sigma_g$ and

13

$4^b\Sigma_g \rightarrow 5^a\Sigma_u$ configurations mainly produce two excited states. The constructive mixing is predicted at 1.04 eV with high oscillator strength, whereas the destructive mixing is predicted at 1.56 eV with low oscillator strength. We also note that as the amount of HFX increases further in the functional, constructive mixing gains more intensity whereas the intensity of destructive mixing becomes much smaller compared to the former. With B3LYP-60%, the intensity of the excited state that originates from the constructive mixing at the 0.40 nm gap distance is quite similar to the intensity obtained for 0.75 nm (Table 3) or 1.00 nm gap distances.

Figure 8. a) Calculated spectra for Ag_8 atomic wire dimers at 0.40 nm gap distances with different functionals of varying HFX. b) The gap distance dependence of calculated spectra for Ag_8 atomic wire dimers with the B3LYP-60% functional.

At this point, it is clear that the splitting of CTP and BDP modes for the longitudinal polarization, which mainly arises from destructive or constructive coupling of configurations, is most pronounced when GGA functionals are employed for the nanowire dimers. This splitting is less obvious as the amount of HFX increases in the functional, especially with the functionals where the off-diagonal coupling element is predicted to be negative. In these cases, a dominant high-intensity peak is predicted for both small and large separation distances. These results can be illustrated more profoundly in Figure 8b, where we show the distance dependence of the absorption spectra for the Ag_8 dimer calculated with B3LYP-60%. With this functional, no significant splitting of the longitudinal peak is observed for the range of 0.30-1.00 nm gap distances, unlike the case in local GGA functionals. In this case, the longitudinal peak shows a continuous red-shift as the gap distance become smaller, which is in fact qualitatively in good agreement with the classical predictions of plasmon coupling. In Figure S4, we show the distance dependence of this redshift for 0.30-1.00 nm gap distance calculated with the B3LYP-60% functional.

Table 4. The Effect of HFX Percentage in the Functional on the Calculated Excited States for Ag_8 Dimers at 0.40 nm Gap Distance
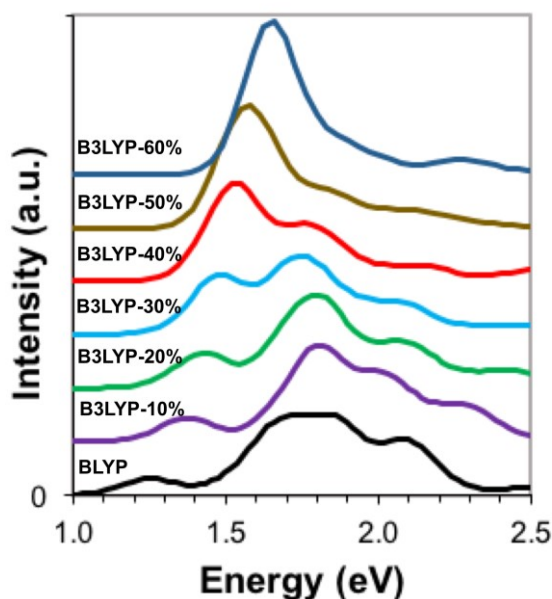
Excited State #	Energy (eV)	Oscillator Strength (a.u.)	Transitions	Weight	Contribution to Transition Dipole Moment
			BLYP		
1	0.74	1.37	$4^a\Sigma_u \rightarrow 5^b\Sigma_g$	0.66	12.32
			$4^b\Sigma_g \rightarrow 5^a\Sigma_u$	0.29	-3.69
2	0.99	1.12	$4^a\Sigma_u \rightarrow 5^b\Sigma_g$	0.16	5.30
			$4^b\Sigma_g \rightarrow 5^a\Sigma_u$	0.11	1.98
3	1.16	1.43	$4^b\Sigma_g \rightarrow 5^a\Sigma_u$	0.32	3.12
			$4^a\Sigma_u \rightarrow 5^b\Sigma_g$	0.13	4.37
			B3LYP-20%		
1	0.91	2.82	$4^a\Sigma_u \rightarrow 5^b\Sigma_g$	0.97	-13.18
			$4^b\Sigma_g \rightarrow 5^a\Sigma_u$	0.02	1.86
2	1.24	1.30	$4^b\Sigma_g \rightarrow 5^a\Sigma_u$	0.72	5.95
			$4^a\Sigma_u \rightarrow 5^b\Sigma_g$	0.01	0.59
3	1.40	0.25	$4^b\Sigma_g \rightarrow 5^a\Sigma_u$	0.14	2.33
			$4^a\Sigma_u \rightarrow 5^b\Sigma_g$	0.01	0.51
			B3LYP-40%		
1	1.04	4.21	$4^a\Sigma_u \rightarrow 5^b\Sigma_g$	0.91	11.39
			$4^b\Sigma_g \rightarrow 5^a\Sigma_u$	0.05	1.17
2	1.56	0.44	$4^b\Sigma_g \rightarrow 5^a\Sigma_u$	0.85	-7.06
			$4^a\Sigma_u \rightarrow 5^b\Sigma_g$	0.06	4.08
			B3LYP-60%		
1	1.09	4.70	$4^a\Sigma_u \rightarrow 5^b\Sigma_g$	0.74	9.42
			$4^b\Sigma_g \rightarrow 5^a\Sigma_u$	0.17	2.96
2	1.94	0.21	$4^b\Sigma_g \rightarrow 5^a\Sigma_u$	0.69	-6.99
			$4^a\Sigma_u \rightarrow 5^b\Sigma_g$	0.13	4.47

It is important to assess how inclusion of HFX affects the optical response of Ag_{41}^{-1} dimers in order to understand the size evolution of the interaction picture shown for Ag_8 dimers. Unfortunately, using the standard formalism of TDDFT with hybrid functionals was not feasible for Ag_{41}^{-1} dimers. Therefore, we have employed the simplified TDDFT formalism (sTDDFT), which is an approximate TDDFT method by Grimme and coworkers.[76] The comparison of sTDDFT and TDDFT is given in Figure S5 for the spectra of Ag_8 dimers calculated with hybrid functionals. The results show a very good agreement between the two methods for Ag_8 dimers. In Figure 9, we show the calculated spectra for Ag_{41}^{-1} dimers using sTDDFT and the B3LYP functional with varying exchange for 0.40 nm gap distance. Again, we have employed the BLYP functional for the HFX=0% case. Similar to the Ag_8 dimers, the calculated spectra show significant differences for the longitudinal peak as the amount of HFX increases in the functional. With BLYP, the spectra mainly exhibit four features around 1.3, 1.7, 1.9 and 2.1 eV. When the amount of HFX is 20%, the features at 1.7 and 1.9 eV merge into a single peak. On the other hand, the peak at 1.3 eV shows a slight blueshift with increase in intensity, whereas the peak at 2.1 eV becomes less intense. As the amount of HFX increases further in the functional, the low-energy peak becomes blue-shifted with increasing intensity continuously, whereas the other features become less intense. For B3LYP-50% and B3LYP-60%, this low-energy peak finally becomes the dominant feature in the spectra.

Overall, the results for Ag_{41}^{-1} dimers regarding the effect of HFX in the level of theory are quite similar to those obtained for the Ag_8 nanowires. In both cases, local GGA functionals predict

the emergence of CTP modes around a gap distance of 0.4-0.6 nm. These results are generally in agreement with previous theoretical work that employs the jellium model[27,28] or atomistic methods for nanoparticle dimers.[58] From a strictly configuration-interaction standpoint, our results indicate that the CTP mode results from destructive coupling of high-intensity transitions whereas the BDP mode results from constructive coupling of the same transitions. The energies and intensities of these modes depend on the off-diagonal coupling between these configurations. Inclusion of HFX exchange in the functional alters the off-diagonal coupling element significantly. As a result, the CTP and BDP modes mainly merge into a single resonance continuously as the amount of HFX increases in the level of theory.

Figure 9. Calculated spectra for Ag_{41}^{-1} nanorod dimers at 0.40 gap distances using sTDDFT and functionals with varying HFX.

It is a well-known issue that GGA and LDA (HFX=0%) functionals suffer from too much delocalization due to the self-interaction error.[79] For excited state calculations of molecular systems, these errors particularly exhibit themselves in charge-transfer phenomena between donor-acceptor systems or molecular aggregates, where (semi)-local functionals often predict spurious charge-transfer states or charge-transfer states with too low energy.[79,80] These problems are often cured by including a significant percentage of HFX either with standard hybrids or range-separated hybrids. In that sense, our results for the optical response of the dimer systems, which suggest that the CTP and BDP modes mainly merge into a single peak with the functionals with 50% or more HFX, are analogous to previous work with molecular aggregates.[63] On the other hand, experimental evidence for the plasmonic assemblies often suggests the emergence of a CTP mode for short separation distances.[37,38] We note that while the nanorods employed in this study generally serve as suitable models for understanding quantum effects on the plasmonic systems, they are much smaller in size than the investigated nanoclusters in experimental work. It is possible that some of the results obtained in this work might be valid for only certain sizes of nanoclusters where quantum effects dominate the optical response. Additionally, shapes and symmetries of the assemblies might play an important role for the emergence of CTP. Nevertheless, our results show

that there are still important questions regarding how HFX affect the coupling between two nanoclusters in the quantum regime. We are planning to address some of these issues in the future.

Conclusion

In summary, we have performed a TDDFT investigation of plasmon coupling for the dimer assemblies of Ag_8 nanowires and Ag_{41}^{-1} nanorods using GGA and hybrid functionals. Our results with GGA functionals show that the splitting of the longitudinal peak in dimer assemblies is closely related to the bonding or antibonding interactions between monomeric orbitals. For long separation distances where the wave-function overlap is very close to zero, the constructive coupling between different excited configurations results in a high-intensity bonding dipole plasmon (BDP) mode. In comparison, destructive coupling of same configurations results in excited states with very small oscillator strengths due to cancellation of dipole moments. For short gap distances such as 0.40 nm, configuration interaction is altered due to wave-function overlap between monomers, and both constructive and destructive mixing of configurations yield significant oscillator strength for both nanowire and nanorod dimers. Calculated transition-fit densities for the excited states indicate that the destructive mixing of configurations shows more charge-transfer plasmon (CTP) character whereas constructive mixing shows more BDP character for such distances.

When hybrid functionals with varying HFX are employed, the calculated optical response of dimers exhibits significant changes compared to the case with GGA functionals. The results are more pronounced for hybrid functionals that include 50% or more HFX, where CTP and BDP modes merge into a single peak in the spectra. We show that these changes are closely related to the coupling element between different configurations that contributes largely to the longitudinally polarized excited states. Our results indicate that the charge-transfer phenomena for plasmon coupling needs to be addressed carefully using hybrid functionals or range-separated functionals as these functionals are known to be more suitable for such cases compared to the semi-local functionals that are generally employed to understand the quantum effects in plasmon coupling.

REFERENCES

1   Y. Y. Yu, S. S. Chang, C. L. Lee and C. R. C. Wang, *J. Phys. Chem. B*, 1997, **101**, 6661–6664.

2   S. Link, M. B. Mohamed and M. A. El-Sayed, *J. Phys. Chem. B*, 1999, **103**, 3073–3077.

3   C. Burda, X. B. Chen, R. Narayanan and M. A. El-Sayed, *Chem. Rev.*, 2005, **105**, 1025–1102.

4   H. Wang, D. W. Brandl, P. Nordlander and N. J. Halas, *Acc. Chem. Res.*, 2007, **40**, 53–62.

5   S. Eustis and M. A. El-Sayed, *Chem. Soc. Rev.*, 2006, **35**, 209–217.

6   K. L. Kelly, E. Coronado, L. L. Zhao and G. C. Schatz, *J. Phys. Chem. B*, 2003, **107**, 668–677.

7   Y. Y. Ma, W. Y. Li, E. C. Cho, Z. Y. Li, T. K. Yu, J. Zeng, Z. X. Xie and Y. N. Xia, *ACS Nano*, 2010, **4**, 6725–6734.

8   B. N. Khlebtsov and N. G. Khlebtsov, *J. Phys. Chem. C*, 2007, **111**, 11516–11527.

9   G. T. Bae and C. M. Aikens, *J. Phys. Chem. C*, 2012, **116**, 10356–10367.

10   I. H. El-Sayed, X. H. Huang and M. A. El-Sayed, *Nano Lett.*, 2005, **5**, 829–834.

11   X. H. Huang, I. H. El-Sayed, W. Qian and M. A. El-Sayed, *J. Am. Chem. Soc.*, 2006, **128**, 2115–2120.

12   P. K. Jain, I. H. El-Sayed and M. A. El-Sayed, *Nano Today*, 2007, **2**, 18–29.

13   C. X. Yu and J. Irudayaraj, *Anal. Chem.*, 2007, **79**, 572–579.

14   R. A. Sperling, P. Rivera gil, F. Zhang, M. Zanella and W. J. Parak, *Chem. Soc. Rev.*, 2008, **37**, 1896–1908.

15   L. G. Xu, H. Kuang, L. B. Wang and C. L. Xu, *J. Mater. Chem.*, 2011, **21**, 16759–16782.

16   M. Stratakis and H. Garcia, *Chem. Rev.*, 2012, **112**, 4469–4506.

17   K. Saha, S. S. Agasti, C. Kim, X. N. Li and V. M. Rotello, *Chem. Rev.*, 2012, **112**, 2739–2779.

18   V. Myroshnychenko, J. Rodriguez-Fernandez, I. Pastoriza-Santos, A. M. Funston, C. Novo, P. Mulvaney, L. M. Liz-Marzan and F. J. G. de Abajo, *Chem. Soc. Rev.*, 2008, **37**, 1792–1805.

19   S. M. Morton, D. W. Silverstein and L. Jensen, *Chem. Rev.*, 2011, **111**, 3962–3994.

20   J. M. McMahon, S. K. Gray and G. C. Schatz, *Phys. Rev. Lett.*, 2009, **103**, 4.

21   C. Oubre and P. Nordlander, *J. Phys. Chem. B*, 2004, **108**, 17740–17747.

22   P. K. Jain, S. Eustis and M. A. El-Sayed, *J. Phys. Chem. B*, 2006, **110**, 18243–18253.

23   P. Nordlander, C. Oubre, E. Prodan, K. Li and M. I. Stockman, *Nano Lett.*, 2004, **4**, 899–903.

24   Y. P. Wu and P. Nordlander, *J. Phys. Chem. C*, 2010, **114**, 7302–7307.

25   W. Q. Zhu, R. Esteban, A. G. Borisov, J. J. Baumberg, P. Nordlander, H. J. Lezec, J. Aizpurua and K. B. Crozier, *Nat. Commun.*, 2016, **7**, 11495.

26   D. Xu, X. Xiong, L. Wu, X. F. Ren, C. E. Png, G. C. Guo, Q. H. Gong and Y. F. Xiao, *Adv. Opt. Photonics*, 2018, **10**, 703–756.

27   J. Zuloaga, E. Prodan and P. Nordlander, *Nano Lett.*, 2009, **9**, 887–891.

28   R. Esteban, A. G. Borisov, P. Nordlander and J. Aizpurua, *Nat. Commun.*, 2012, **3**, 805.

29   A. Varas, P. Garcia-Gonzalez, J. Feist, F. J. Garcia-Vidal and A. Rubio, *Nanophotonics*, 2016, **5**, 409–426.

30   R. Sinha-Roy, P. Garcia-Gonzalez, H. C. Weissker, F. Rabilloud and A. I. Fernandez-

Dominguez, *Acs Photonics*, 2017, **4**, 1484–1493.

31   K. H. Su, Q. H. Wei, X. Zhang, J. J. Mock, D. R. Smith and S. Schultz, *Nano Lett.*, 2003, **3**, 1087–1090.

32   T. Atay, J. H. Song and A. V Nurmikko, *Nano Lett.*, 2004, **4**, 1627–1631.

33   P. K. Jain and M. A. El-Sayed, *J. Phys. Chem. C*, 2008, **112**, 4954–4960.

34   N. J. Halas, S. Lal, W. S. Chang, S. Link and P. Nordlander, *Chem. Rev.*, 2011, **111**, 3913–3961.

35   E. Prodan, C. Radloff, N. J. Halas and P. Nordlander, *Science (80-.).*, 2003, **302**, 419–422.

36   B. Willingham, D. W. Brandl and P. Nordlander, *Appl. Phys. B-Lasers Opt.*, 2008, **93**, 209–216.

37   K. J. Savage, M. M. Hawkeye, R. Esteban, A. G. Borisov, J. Aizpurua and J. J. Baumberg, *Nature*, 2012, **491**, 574–577.

38   S. F. Tan, L. Wu, J. K. W. Yang, P. Bai, M. Bosman and C. A. Nijhuis, *Science*, 2014, **343**, 1496–1499.

39   W. Ekardt, *Phys. Rev. B*, 1985, **32**, 1961–1970.

40   W. Ekardt, *Phys. Rev. B*, 1985, **31**, 6360–6370.

41   M. Brack, *Rev. Mod. Phys.*, 1993, **65**, 677–732.

42   E. Prodan and P. Nordlander, *Chem. Phys. Lett.*, 2002, **352**, 140–146.

43   E. Prodan, P. Nordlander and N. J. Halas, *Chem. Phys. Lett.*, 2003, **368**, 94–101.

44   E. Prodan and P. Nordlander, *Nano Lett.*, 2003, **3**, 543–547.

45   E. Prodan, P. Nordlander and N. J. Halas, *Nano Lett.*, 2003, **3**, 1411–1415.

46   R. Baer, D. Neuhauser and S. Weiss, *Nano Lett.*, 2004, **4**, 85–88.

47   C. M. Aikens, S. Z. Li and G. C. Schatz, *J. Phys. Chem. C*, 2008, **112**, 11272–11279.

48   H. E. Johnson and C. A. Aikens, *J. Phys. Chem. A*, 2009, **113**, 4445–4450.

49   G. Barcaro, M. Broyer, N. Durante, A. Fortunelli and M. Stener, *J. Phys. Chem. C*, 2011, **115**, 24085–24091.

50   N. Durante, A. Fortunelli, M. Broyer and M. Stener, *J. Phys. Chem. C*, 2011, **115**, 6277–6282.

51   E. Townsend and G. W. Bryant, *Nano Lett.*, 2012, **12**, 429–434.

52   X. Lopez-Lozano, C. Mottet and H. C. Weissker, *J. Phys. Chem. C*, 2013, **117**, 3062–3068.

53   E. B. Guidez and C. M. Aikens, *J. Phys. Chem. C*, 2013, **117**, 12325–12336.

54   N. V Ilawe, M. B. Oviedo and B. M. Wong, *J. Chem. Theory Comput.*, 2017, **13**, 3442–3454.

55   O. A. Douglas-Gallardo, G. J. Soldano, M. M. Mariscal and C. G. Sanchez, *Nanoscale*, 2017, **9**, 17471–17480.

56   J. Vincenot and C. M. Aikens, in *Advances in the Theory of Atomic and Molecular Systems*, eds. P. Piecuch, J. Maruani, G. Delgado-Barrio and S. Wilson, Springer Netherlands, 2009, vol. 20, p. 253−264.

57   G. T. Bae and C. M. Aikens, *J. Phys. Chem. A*, 2012, **116**, 8260–8269.

58   J. M. Fitzgerald, S. Azadi and V. Giannini, *Phys. Rev. B*, 2017, **95**, 235414.

59   F. Alkan and C. M. Aikens, *J. Phys. Chem. C*, 2018, **122**, 23639–23650.

60   A. Dreuw, J. L. Weisman and M. Head-Gordon, *J. Chem. Phys.*, 2003, **119**, 2943–2946.

61   A. Dreuw and M. Head-Gordon, *J. Am. Chem. Soc.*, 2004, **126**, 4007–4016.

62   A. Dreuw and M. Head-Gordon, *Chem. Rev.*, 2005, **105**, 4009–4037.

63   R. J. Magyar and S. Tretiak, *J. Chem. Theory Comput.*, 2007, **3**, 976–987.

64   C. Adamo and D. Jacquemin, *Chem. Soc. Rev.*, 2013, **42**, 845–856.

65   E. B. Guidez and C. M. Aikens, *Nanoscale*, 2014, **6**, 11512–11527.

66   C. F. Guerra, J. G. Snijders, G. te Velde and E. J. Baerends, *Theor. Chem. Acc.*, 1998, **99**, 391–403.

67   G. te Velde, F. M. Bickelhaupt, E. J. Baerends, C. F. Guerra, S. J. A. Van Gisbergen, J. G. Snijders and T. Ziegler, *J. Comput. Chem.*, 2001, **22**, 931–967.

68   ADF2017, *SCM, Theor. Chem. Vrije Univ. Amsterdam, Netherlands, http//www.scm.com.*

69   A. D. Becke, *Phys. Rev. A*, 1988, **38**, 3098–3100.

70   J. P. Perdew, *Phys. Rev. B*, 1986, **33**, 8822–8824.

71   J. P. Perdew, K. Burke and Y. Wang, *Phys. Rev. B*, 1996, **54**, 16533–16539.

72   A. D. Becke, *J. Chem. Phys.*, 1993, **98**, 5648–5652.

73   C. T. Lee, W. T. Yang and R. G. Parr, *Phys. Rev. B*, 1988, **37**, 785–789.

74   E. B. Guidez and C. M. Aikens, *Nanoscale*, 2012, **4**, 4190–4198.

75   S. Grimme, *J. Chem. Phys.*, 2013, **138**, 244104.

76   C. Bannwarth and S. Grimme, *Comput. Theor. Chem.*, 2014, **1040**, 45–53.

77   P. K. Jain and M. A. El-Sayed, *Chem. Phys. Lett.*, 2010, **487**, 153–164.

78   E. B. Guidez and C. M. Aikens, *Phys. Chem. Chem. Phys.*, 2014, **16**, 15501–15509.

79   J. Autschbach and M. Srebro, *Acc. Chem. Res.*, 2014, **47**, 2592–2602.

80   J. Autschbach, *CHEMPHYSCHEM*, 2009, **10**, 1757–1760.